Research Article | Vol. 10, No. 3 | 1 Mar 2019 | BIOMEDICAL OPTICS EXPRESS 1482
Biomedical Optics EXPRESS

Dynamic optical coherence tomography imaging of the lacrimal passage with an extrinsic contrast agent

REIKO YOSHIMURA,[1,*] DONG-HAK CHOI,[1] MASAHIRO FUJIMOTO,[2] AKIHITO UJI,[2] FUMIKO HIWATASHI,[3] AND KOHJI OHBAYASHI[3,4]

[1]*Center for Natural Science, Kitasato University, 1-15-1 Kitazato, Minami, Sagamihara, Kanagawa 252-0374, Japan*
[2]*Department of Ophthalmology and Visual Sciences, Kyoto University, Yoshida-honmachi, Sakyo-ku, Kyoto 606-8501, Japan*
[3] *Systems Engineering Inc., 2-19-24 Honkomagome, Bunkyo-ku, Tokyo 113-0021, Japan*
[4]*Advanced Imaging Co. Ltd., 2-23-9 Someino, Sakura, Chiba 285-0831, Japan*
r.yoshi@kitasato-u.ac.jp

Abstract: Recently, *in vivo* trans-conjunctiva optical coherence tomography (OCT) imaging of the lacrimal passage was demonstrated using a turbid commercial eye drop as an extrinsic contrast agent. However, static OCT images are not sufficient to unambiguously delineate the lumen boundary to render 3D lumen images of the lacrimal passage by segmentation. The turbid eye drop is expected to include small particles that flow and undergo Brownian motion and can be used as an extrinsic contrast agent for dynamic OCT. We conducted dynamic OCT measurements of the lacrimal passage using a swept source OCT system. Firstly, characterization of the dynamic OCT properties of the eye drop was performed. For improved delineation of the lumen boundary, we calculated the sum of the squared differences of intensities with two different normalization parameters. By making composite color images from OCT images and these two dynamic OCT images, we could execute unambiguous segmentation of the lumen of the lacrimal passage. Three-dimensional volumetric images of parts of the lacrimal passage, i.e., lacrimal canaliculus and lacrimal punctum, are demonstrated.

1. Introduction

In this study, the human lacrimal punctum (LP) and lacrimal canaliculus (LC) of the lacrimal drainage system were imaged using dynamic optical coherence tomography (D-OCT). The human lacrimal drainage system of the right eye is depicted schematically in Fig. 1 [1]. Tears are produced at the lacrimal gland, cover the surface of the cornea as film, then drained through the LPs. The LPs, which are inlets of LCs, are located at the backside rim of the superior and inferior eyelids. The LCs pass vertically from the rim of the lids, change direction, and extend horizontally. Two LCs unite to form the common canaliculus in most cases. The combined canaliculus leads to the lacrimal sac and nasolacrimal duct. Tears are then drained into the nose. Vision quality is affected by the stability of the tear film. Morphological disorders in the lacrimal drainage system lead to instability of the tear film, e.g., watery eye disease is caused by lacrimal canaliculus obstruction. A punctal plug is often used for the treatment of dry eye by controlling the out flow of tears. However, problems, such as the plug falling off, occur sometimes and, although rare, the plug even moves into an LC, which requires surgery. A precise morphological determination of the 3D volumetric structure of the punctum and use of a properly shaped punctal plug may decrease the occurrence of such problems. These examples show the clinical usefulness of morphological imaging of the lacrimal drainage system.

#355026 https://doi.org/10.1364/BOE.10.001482
Journal © 2019 Received 10 Dec 2018; revised 31 Jan 2019; accepted 31 Jan 2019; published 28 Feb 2019

Biomedical Optics EXPRESS

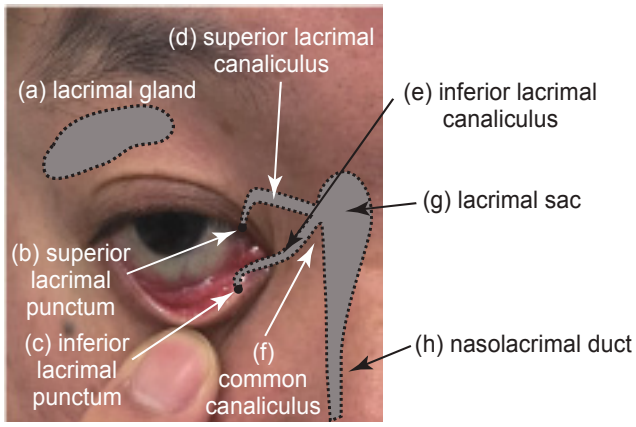

Fig. 1. Photograph of eye and schematic depiction of lacrimal drainage system. To image the lacrimal canaliculus (LC) in the conjunctiva, the inferior eyelid is flipped to expose it. (a): lacrimal gland, (b): superior lacrimal punctum (LP), (c): inferior LP, (d): superior LC, (e): inferior LC, (f): common canaliculus, (g): lacrimal sac, (h): nasolacrimal duct.

Fujimoto et al. recently demonstrated clear OCT imaging of an LC with and without a contrast agent [2]. Flipping of the eyelid, as illustrated in Fig. 1, enables OCT imaging of the conjunctiva and tissue morphology inside it. By imaging through the conjunctiva, an LC could be distinctly imaged as a hypo-intensity region because of weak light scattering of the mucosa and tear. They could further image the lumen of the LC by applying a turbid eye drop as a contrast agent before imaging to partially replace tears with it. Compared with an example of OCT imaging restricted only near an LP [3], the study by Fujimoto et al. was a tremendous improvement in OCT imaging of the lacrimal drainage system. They called the imaging procedure OCT dacryography (OCT-D) to distinguish it from OCT angiography (OCT-A).

Although OCT-D is sufficient to image the mucosa wall and lumen of an LC, it is sometimes difficult to distinguish the lumen of an LP (or LC) and surrounding tissue. To enhance OCT-D capability, we conducted dynamic OCT-D (D-OCT-D) in this study. The turbid eye drop includes particles that undergo Brownian motion to drive dynamic enhancement of OCT-D. By D-OCT-D imaging, we could unambiguously delineate the lumen of an LP and LC, and make a 3D rendering of them. All our imaging was done through the conjunctiva. We have attempted the LC imaging from outside of the skin, but it was failed even with the contrast agent. The lacrimal sac could not be imaged. Our imaging in this work was limited to the lower LP and LC because of ease of flipping the eyelid.

2. Methods

2.1 Experimental system

Figure 2 shows the experimental configuration of our swept-source OCT (SS-OCT) system. The SS was a commercial reflective Fabry-Perot tunable laser (RFPTL) (1310nm-SS, Axsun Technologies, USA). The laser was operated at a tuning rate of 50 kHz. The average power measured with an optical power meter (PM20, Thorlabs Japan) at the laser output was 12.5 mW. This power was attenuated to 8.6 mW at the output of the sample arm by optical components of the interferometer. This illuminating power slightly exceeds the maximum permissible exposure (MPE) regulated by ANSI [4]. Therefore, we took care only to illuminate conjunctiva and skin, strictly avoiding direct illumination to the pupil and iris as done by Fujimoto et al. [2]. The center wavelength was 1300 nm and the sweep width was 140 nm. The effective wavelength span we used was 137 nm and the axial resolution obtained with Hanning window apodization was 10 μm. The output of the light source was divided

Biomedical Optics EXPRESS

using a coupler (CP1) (Opneti Communications, China) to the reference arm (20%) and sample arm (80%). The sample arm light illuminated the volunteer through an optical circulator (CRS) (Opneti Communications, China), collimator lens (CLS), and objective lens (OLS). A galvano mirror (GM) (model 6210, Cambridge Technology, USA) was used to scan the light beam on the sample in the two lateral directions. From a beam diameter of about 4 mm from the CLS and the focal length of the OLS, the lateral resolution was 21 μm at focal point. Backscattered or back reflected light from the sample was collected with the illuminating optics. The reference arm was composed of a circulator (CRR) (Opneti Communications, China), collimator (CLR), objective lens (OLR), and reference mirror (RM). Light from the reference arm and sample arm interfered at another coupler (CP2) (Opneti Communications, China) of a 50:50 split ratio. The polarization of light in the sample and reference arms were adjusted with polarization controllers PCS and PCR (FPC030, Thorlabs Japan). The interference light from CP2 was detected with a balanced photo receiver (BPR) (PDB420C, Thorlabs Japan), and its bandwidth was 75 MHz. The output from the BPR was analog-to-digital (A/D) converted using a data acquisition (DAQ) board (ATS9462, Alazer Tech, Canada) and acquired using a computer (Endeavor Pro 4000, EPSON, Japan). The GM was controlled using a D/A converter (PCI-6733, NI Japan). The OCT coherence length measured at 6-dB reduction of the point spread function was 4.4 mm. The sensitivity of the system measured at an OCT depth of 0.1 mm was 110 dB. Our system is slightly different from ordinary anterior segment OCT systems. The optical axis of the illuminating beam direction is tilted by about 45 degrees from the horizontal direction, as shown in Fig. 2(b). The volunteer sat on a chair and flipped his or her eyelid with a finger to expose the conjunctiva.

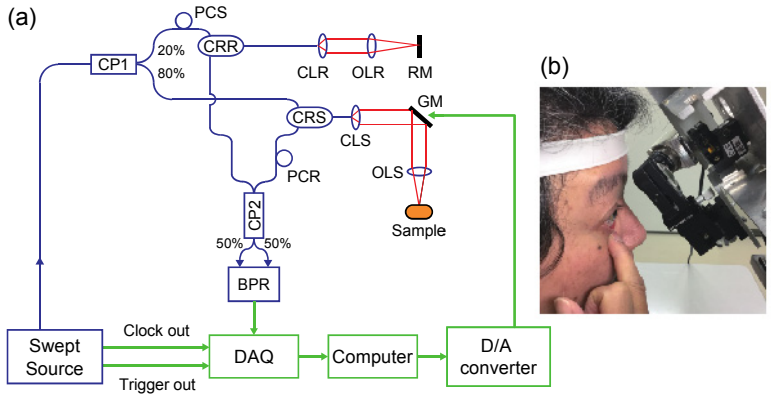

Fig. 2. (a) Experimental set up for SS-OCT system. CP1 and CP2: couplers, CRR and CRS: circulators, PCR and PCS: polarization controllers, DAQ: data acquisition board, D/A converter: digital-to-analog converter, CLR and CLS: collimator, OLR and OLS: lens, BPR: balanced photo receiver, GM: galvano mirror. (b) Direction of illuminating beam out of the OCT system is tilted about 45 degrees from the horizontal to focus on the conjunctiva of the volunteer with the objective lens (OLS). The volunteer flips his eyelid with his finger to expose the conjunctiva.

2.2 Data processing

The OCT interference signals contain intensity and phase information. Dynamic variations of the OCT image can be calculated using either one or both. Recently, a comprehensive review of OCT-A was reported by Chen and Wang [5]. According to the report, OCT-A methods using phase information are sensitive to motion artifacts. As shown in Figs. 1 and 2(b), the eyelid was flipped using a finger in this study, and motion artifacts may arise due to involuntary small movement of the finger, as well as the volunteer's head. Therefore,

Biomedical Optics EXPRESS

intensity-signal-based D-OCT analyses without using phase information were used in this study to reduce the effects from motion artifacts.

Several intensity-signal-based OCT-A methods have been proposed and demonstrated. The D-OCT-D method is different from angiography method, but the same data processing with that of OCT-A can be applied to it. Barton and Stromski [6] visualized 2D images of vessels of a hamster from the spectral speckle of the in vivo OCT image without using phase information. Mariampillai et al. demonstrated the statistical calculation of the variance in intensity to effectively visualize flow and developed method called speckle variance OCT-A (SV-OCT-A) [7,8]. Jonathan et al. [9] and Enfield et al. [10] proposed the correlation mapping method. Correlations of the variation in intensity at each pixel between different frames were calculated with this method. In their calculation, the correlation was normalized by intensity, enhancing speckle variations at pixels having weak OCT signals, i.e., deeper region of tissues. This normalization evidently has a side effect to enhance meaningless correlation variation at the noise floor, which exhibits the smallest intensity. To eliminate such artifacts, they devised a thresholding procedure and separated out a noise-floor image to obtain a meaningful flow image only. Subsequently, Jia et al. [11] proposed the split-spectrum amplitude decorrelation angiography method (SSADA). In contrast to the correlation mapping method, this method measures the decorrelation of the speckle signals between two consecutive B-scans. With the method, an A-scan interference signal of an SS-OCT system is split into several parts with Gaussian windows, reducing effective data acquisition time; thus, reducing motion artifacts. The axial alignment between B-scans can be done effectively with this process.

We used slightly different data processing from those described above while taking advantage of the benefits of the former methods. The data-acquisition procedure is shown in Fig. 3(a). In an A-scan along depth z-direction, data were acquired at 1600 wavenumber points and FFT was performed at 4096 zero-padded data points, a half of which corresponding to the imaging depth range of 5 mm. In a B-scan, 200 A-scans were executed along the lateral x-direction. At the same location of the B-scan, the number of B-scans N (= 4) was acquired. Two hundred of such B-scan sets were acquired along the lateral y-direction. The data-processing procedure is shown in Fig. 3(b). After DC subtraction, we adopted the split spectrum algorithm [11], FFT was performed, thresholding to eliminate the meaningless noise-floor was applied [9,10], and executed axial alignment by using the ordinary cross correlation method. Then, Eq. (1) was calculated using the following procedures for each split spectrum, and the average was calculated. We call this procedure the sum of total squared difference (STSD) for convenience.

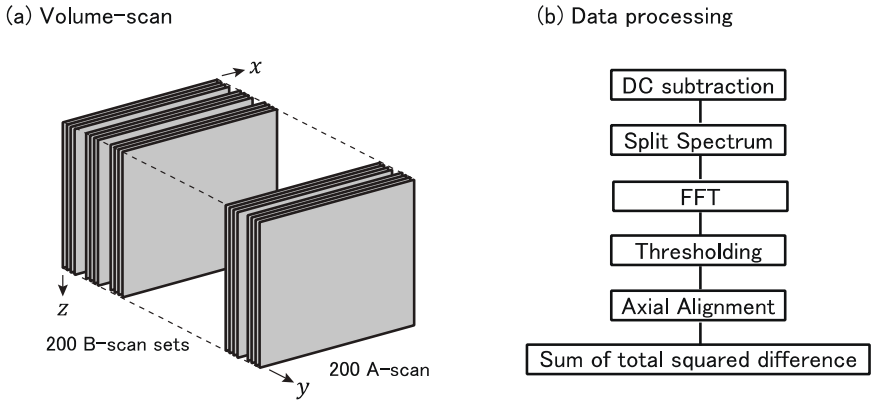

Fig. 3. (a) B-scan was made with 200 A-scans in the lateral x-direction. Four B-scans were acquired as a set at the same location. 200 of such B-scan sets were acquired in the lateral y-direction to complete a volume scan. (b) Data processing flow.

Biomedical Optics EXPRESS

We used the following equation to calculate the D-OCT-D signal $D_\alpha(i,j,k)$:

$$D_\alpha(i,j,k) = \frac{2}{N(N-1)} \sum_{n>m=1}^{N} \frac{\left(I_{i,j,k}(n) - I_{i,j,k}(m)\right)^2}{\left(I^2_{i,j,k}(n) + I^2_{i,j,k}(m)\right)^\alpha} \quad (1)$$

where k is the index of the B-scan set at a lateral y-coordinate, i and j are the lateral and depth pixels indices (x and z coordinates), n and m are different frame numbers in the same B-scan set (i.e. same k), $I_{i,j,k}$ is the amplitude of the complex value of OCT data, and α is the exponent of the normalization coefficient. For a larger value of α the denominator of Eq. (1) shows a steeper decrease as the total sum of the intensity decreases at deeper tissue locations. As a result, $D_\alpha(i,j,k)$ at deeper tissue locations are more enhanced for larger values of α than for smaller values of α. Note that for α = 0, Eq. (1) is close to the conventional SV-OCT signal [7,8]. If only adjacent frames in same k are used for summation with α = 1, Eq. (1) equals to the SSADA [11]. By adding non-adjacent terms, we can increase the signal-to-noise ratio (S/N). The conventional SV-OCT signal is weak at deeper OCT depths because the signal is weak. While SSADA significantly enhances dynamic signals at deeper tissue, projection artifacts of blood vessels sometimes obscured the boundary of the LC image in our particular case. The mucosa wall of an LC exhibits weaker intensity compared with the surrounding tissue and eye-drop suspended tear, and the D-OCT signal of mucosa normalized by the signal power (α = 1) is sometimes too much enhanced. By choosing the normalization factor of α = 0.5, such an effect can be mitigated. By comparing D-OCT-D images calculated with different α values as well as an ordinary OCT image, we can unambiguously delineate the lumen of the lacrimal passage. We conducted D-OCT-D image processing for α = 0.5 and 1.

2.3 Extrinsic contrast agent

Conventional OCT angiography (OCT-A) methods use blood-vessel cells as intrinsic contrast agents [5]. Using extrinsic contrast agents to enhance dynamic signals in OCT has been introduced recently. Intralipid was used as an extrinsic contrast agent for OCT-A by Merkle et al. to image the brain [12] and retinal and choroidal vessels [13] of rats. As mentioned in the Introduction, Fujimoto et al. used the eye drop as an extrinsic contrast agent to enhance the human lacrimal passage [2]. We used the same eye drop, called rebamipide ophthalmic suspension UD2% (hereafter ROS) (Otsuka Pharmaceutical, Japan) to enhance the dynamic OCT dacryography (D-OCT-D) signal. It includes 20 mg of rebamipide in 1 mL of ROS. ROS is routinely prescribed for treatment of dry eye by improving the production of mucin and stabilizing tears; therefore, mitigating keratoconjunctival epithelium disorder. The reason why we used the eye drop ROS instead of more familiar intralipid for extrinsic contrast agent is that the subject is *in vivo* human. Intralipid is routinely used for intravenous drip for human but not used for application to eye surface directly. For conformance to medical ethics, we need to verify safety of the procedure and to get government approval to perform it, the latter usually takes a long time. The routinely used eye drop is safe and ready to use. ROS is turbid and includes suspended particles. Such particles scatter light strongly while flowing or undergoing Brownian motion; thus, enhancement of the dynamic OCT image is expected as well as ordinary OCT signal.

As mentioned above, intralipid cannot be readily used for dynamic OCT dacryography (D-OCT-D) at this time. Researchers of dynamic OCT would be interested to know OCT properties of the eye drop ROS, since it is a new contrast agent. To share reference information on ROS with researchers in the OCT community, we compared OCT images of ROS and 10% intralipid, the latter has been often used as a reference contrast agent of OCT [6,14,15].

Biomedical Optics EXPRESS

Figure 4 shows OCT images of both liquids contained in plastic ampules of the same shape. A photograph of an ampule containing liquid is shown in Fig. 4(a). Figures 4(b) and 4(c) show OCT images of the eye drop ROS and intralipid in ampules along the red line in Fig. 4(a). Figures 4(d) and 4(e) show the intensity profiles of ROS and intralipid along the red dotted lines in Figs. 4(b) and 4(c), respectively, which are the averages of 400 profile signals. Though the scattering intensities near the surface of both liquids were nearly the same, the image-decay rate with the depth of ROS was faster than that of intralipid, as shown in Figs. 4(d) and 4(e). Fitting the A-scan profile to a functional form $I_o\exp(-z/z_p)$, the imaging penetration depths (z_p) of ROS and intralipid were 0.12 and 0.22 mm, respectively. Although the penetration depth decreased, the reduction was not serious enough to prevent observing dynamic OCT dacryography (D-OCT-D) signals for expected lumen size. When applied to the human eye in vivo, ROS may be diluted by tears, and scattering power may be reduced by dilution. The reduction of scattering within the lumen of LC filled with ROS may increase the image intensity of deeper lumen wall and tissue beneath it. Projection artifacts prominent in dynamic imaging of blood vessels are nearly absent for imaging of intralipid [6,14,15]. Considering the similar OCT property of ROS to intralipid, we regard projection artifacts are also negligible in ROS.

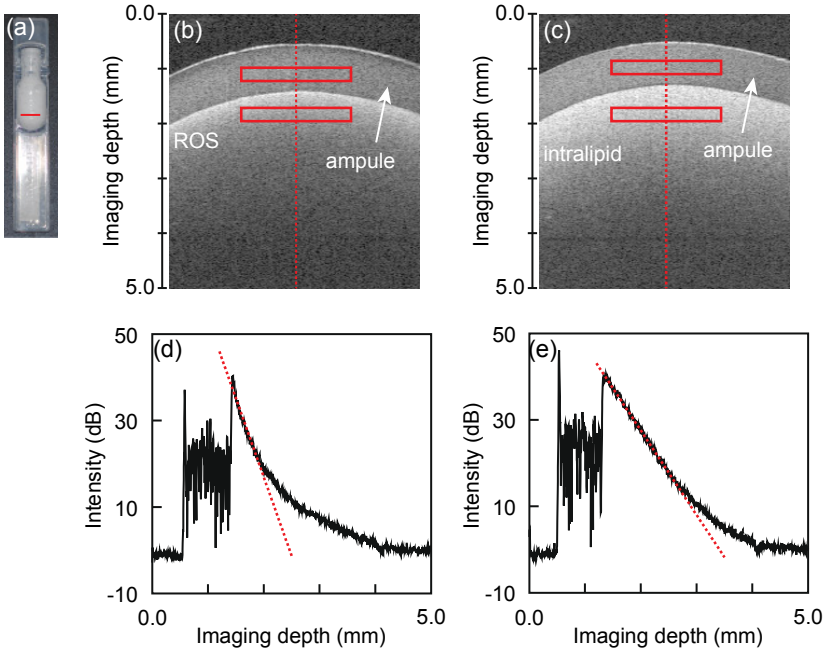

Fig. 4. OCT images of rebamipide ophthalmic suspension UD2% (ROS) and intralipid in the respective ampules. (a) Photograph of ampule containing liquid, where the red line indicates location of B-scan. (b) OCT B-scan image of ROS along the red line in (a). (c) OCT B-scan image of intralipid along the red line in (a). (d) A-scan profile of ROS along the red dotted line in (b). (e) A-scan profile of ROS along the red dotted line in (c).

2.4 Time interval analysis of a dynamic OCT signal

As explained in subsection 2.2, the sum of total squared difference (STSD) calculation, using squared differences not only between adjacent but also all possible pairs, was done for dynamic OCT dacryography (D-OCT-D) imaging. In order to confirm a benefit of this calculation, the time dependence of averaged normalized intensity difference (ANID), defined with the following expression, was calculated:

Biomedical Optics EXPRESS

$$\mathrm{ANID}(n) = \left\langle \frac{\left(I_{i,j,k}(n) - I_{i,j,k}(0)\right)^2}{I^2_{i,j,k}(n) + I^2_{i,j,k}(0)} \right\rangle \tag{2}$$

where <> denotes the average over pixel values within a chosen finite region in the OCT image, and n is the sequential number of the acquired image, which also indicates the time interval when multiplied with that of adjacent image acquisition. A series of B-scans was acquired at the same B-scan location (k is the same). From each B-scan image, the regions indicated with the red rectangles in Figs. 4(b) and 4(c) were selected to calculate the average expressed using Eq. (2). Figures 5(a) and 5(b) respectively show the ANIDs of the eye drop ROS and intralipid as functions of time interval. The ANIDs of the ampules are also plotted in the respective figures. The ANID of the solid ampule wall shows a small constant value of about 0.014, whereas those of ROS and intralipid increased with time interval then reached a saturation value of about 0.21 at a 2-frame interval for intralipid and 4-frame interval for ROS. In the case of ROS, the ANID between adjacent B-scans was 0.16 and increased with time interval, approaching a saturation value of about 0.21. Therefore, we can use larger ANID and improve image quality by including ANID not only between adjacent acquisitions but also all possible pairs in a B-set. In the case of intralipid, ANID was 0.19, even between adjacent acquisitions, the saturation value being about 0.21. Even in this case, inclusion of non-adjacent terms improved the S/N. For the ROS used in this experiment, the improvement in the S/N of ANID was expected by inclusion of non-adjacent terms.

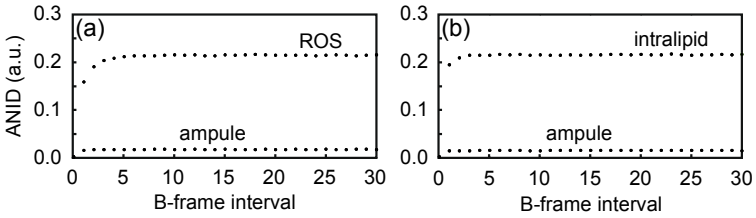

Fig. 5. The dependence of averaged normalized intensity difference (ANID) on B-frame time interval: (a) ROS and (b) intralipid.

The dependence of the averaged normalized intensity difference (ANID) on B-frame acquisition-time interval is more clearly understood by observing A-scan data also. Figures 6(a) and 6(b) show the M-scan OCT images of the eye drop ROS and intralipid in ampules at the same lateral position as functions of A-scan interval. In an M-scan, OCT intensity profiles as a function of depth at the same location, i.e. A-scan, are repeatedly measured as a function of time. If an observed subject is static, M-scan image intensity at a selected fixed depth is nearly constant and exhibits a line image with nearly constant intensity in the direction of A-scan time interval. This is the case of ampule images in Figs. 6(a) and 6(b). On the contrary, if the internal structure of a subject changes with time, the corresponding A-scan profile also changes with time, therefore the M-scan image intensity at a selected fixed depth shows variation. This is the case for images of ROS and intralipid in Figs. 6(a) and 6(b), respectively. Figures 6(c) and 6(d) show ANIDs obtained from data within the section indicated with arrows and thick red bars in Figs. 6(a) and 6(b). Because the number of points within each bar is too small to calculate ANID with sufficient accuracy, we averaged over 150 M-scan images to obtain the plots shown in Figs. 6(c) and 6(d). In our system, the time interval of adjacent A-scans was 1/(50 kHz) = 20 μs, and the time interval between adjacent B-scans was (20 μs) $\times$ (200 + 100 A-scans per B-scan) = 6 ms. The large dots in Figs. 6(c) and 6(d) correspond to the B-frame intervals in Figs. 5(a) and 5(b). The ANID of ROS continued to increase at the second B-frame interval, while that of intralipid nearly saturated at the second B-frame interval.

Biomedical Optics EXPRESS

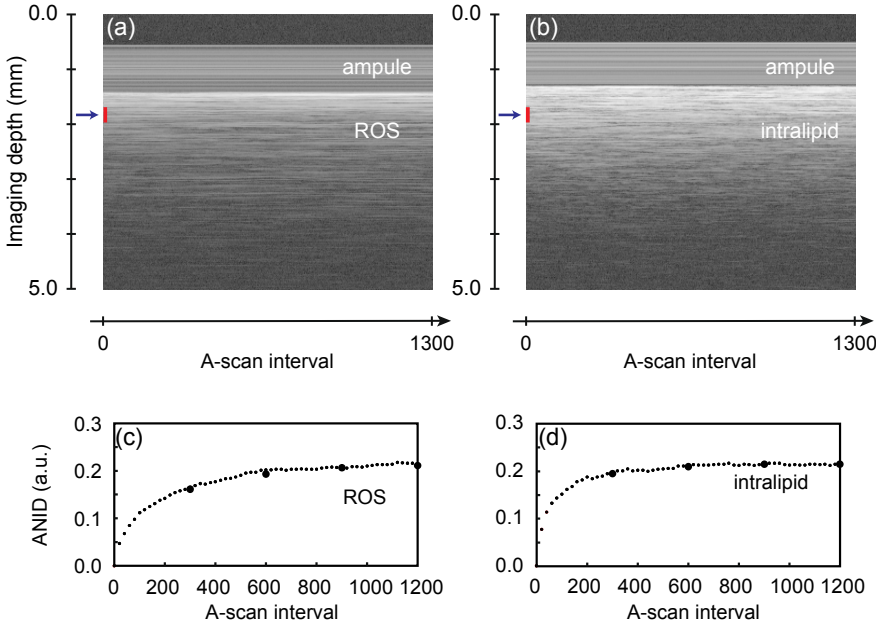

Fig. 6. M-scan images of OCT as functions of A-scan interval: (a) ROS, and (b) intralipid. OCT images of the ampule wall are nearly constant, while those of ROS and intralipid change. The change is slow for ROS compared with that for intralipid. The averaged normalized intensity differences (ANIDs) are plotted as functions of A-scan interval for (c) ROS and (d) intralipid.

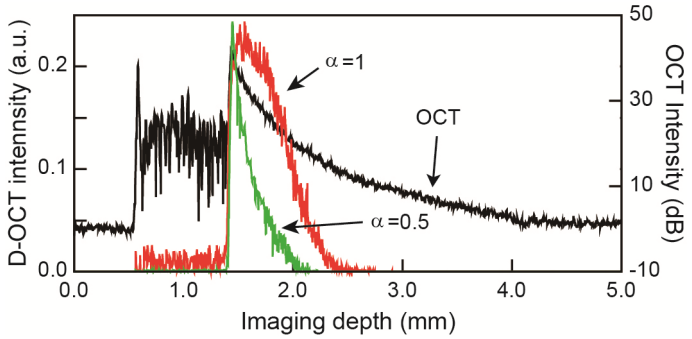

Fig. 7. Comparison of D-OCT A-scan profiles calculated using STSD by selecting different α values: α = 0.5 (green curve), and α = 1 (red curve).

As mentioned above, we adjusted the degree of enhancement by changing α in Eq. (1). Figure 7 shows how the sum of total squared difference (STSD) signal of the eye drop ROS depends on this parameter. The plots were obtained from averages over 100 A-scan profiles of STSD along the red dotted line in Fig. 4(b). As α increased from 0.5 to 1, STSD signals were enhanced at deeper depths; therefore, at weaker intensities. From this plot only, one may conclude that STSD with α = 1 is the best to cut out the LC. However, the LC lumen is surrounded with a mucosal wall, which has a very weak OCT signal; therefore, the mucosal wall should be greatly enhanced with α = 1, as expected from Fig. 7. This enhancement resulted in projection artifact images of blood vessels at the mucosa obscuring the boundary between the mucosa and LC lumen, which should be distinct for delineation of the mucosa. Less enhancement with α = 0.5 made the boundary clear, although dynamic enhancement decreased. The combined use of complementary images resulted in unambiguous segmentation of LP and LC shapes.

Biomedical Optics EXPRESS

3. Lacrimal canaliculi images with contrast agent

3.1 2D Imaging of the lacrimal passage

We acquired 2D and 3D LC images of 45-year-old healthy female volunteer subject with and without ROS as the contrast agent. Kitasato University Hospital's Ethics Committee, in accordance with the tenets of the Declaration of Helsinki, approved the study of human imaging. Volunteers were educated on the purpose of the study and informed consent was obtained from each volunteer before beginning the study. Figure 8(a) shows the scanning area and direction of the OCT measurement. The white box in the figure indicates the scanning area (2.5 mm × 2.5 mm) and the white arrow indicates the B-scan direction. During imaging, the subject flipped the lower eyelid with her finger to expose the LP and conjunctiva. Figure 8(b) shows a B-scan image before application of ROS to the subject. In the trans-conjunctiva image, we can identify the LC as the belt shaped dark area. The LP is located at the top of this image. Although the LC is distinctively imaged as a dark belt, it includes the lumen and surrounding mucosa. Distinction of lumen from the mucosa is partially difficult with this imaging. A B-scan image acquired after application of ROS is shown in Fig. 8(c). The imaging was started about one minute after application of ROS. The location of the cross section is close to that of Fig. 8(b) but not exactly the same. The applied ROS flowed through the LC mixed with tear and significantly enhanced the image of the LC lumen. The dark area around the enhanced lumen is the mucosa. This enhancement of the lumen image was first demonstrated by Fujimoto et al. [2]. In depicting these B-scans, refractive index correction was applied vertically to all images, assuming the representative tissue refractive index of 1.43.

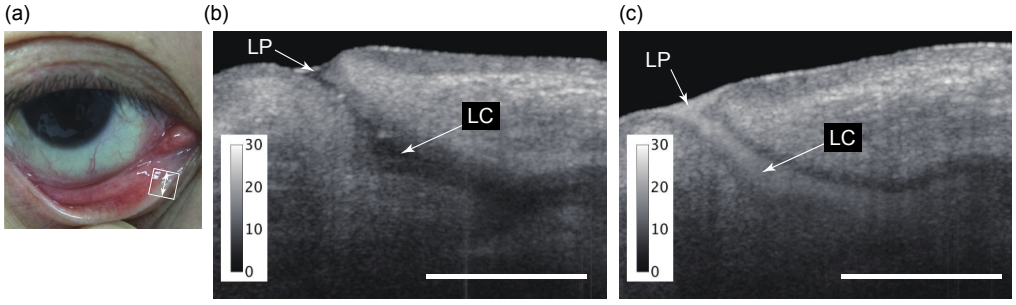

Fig. 8. (a): Photograph of the eyelid and LP showing the OCT scanning area (white rectangle representing an area of 2.5 mm × 2.5 mm), (b): OCT image of the LC before using ROS, (c): OCT image of the LC after using ROS. White arrows in (b) and (c) indicate the LP and LC. Scale bars in (b) and (c) are 1 mm. The gray scale bars indicate OCT signal power in dB.

Figures 9(a)-9(c) were imaged immediately after applying ROS to the volunteer. Figure 9(a) shows the OCT image, and Figs. 9(b) and 9(c) show the STSD images calculated using α = 0.5 and 1, respectively. In all STSD images, thresholding was applied in order to reduce noise exceeding the threshold of 2.5 over the noise floor of OCT image. Figures 9(d-I) and 9(d-II) are the A-scan profiles corresponding to the white dashed lines (I) and (II) in Figs. 9(a)-9(c), respectively. The vertical scale of Fig. 9(d) indicates the signal power of the OCT image or STSD images normalized by the maximum value of each plot. The red arrows in Figs. 9(a)-9(c) are corresponding to the red arrows in Figs. 9(d-I) and 9(d-II), respectively. The ROS flowing inside the LC lumen is clear in all images in Figs. 9(a)-9(c). However, the features of lumen-image enhancement differ depending on α. Along the lines labeled I, the lumen images were clearly enhanced in all images (Figs. 9(a)-9(c)), as shown in Fig. 9(d-I). Additionally, the signal from surrounding tissue of the lumen was considerably reduced in the image of (c) (α = 1). The deeper end surface of the lumen image for OCT is blurred in the A-scan profiles along the line labeled II in Fig. 9(d-II). In this figure, the deeper end surface of

Biomedical Optics EXPRESS

the lumen was clearest for α = 0.5. The gray scale bars in Figs. 9(a), 9(b), and 9(c) respectively indicate OCT signal power in dB, STSD (α = 0.5) signal intensity in dB, and STSD (α = 1) signal intensity in linear.

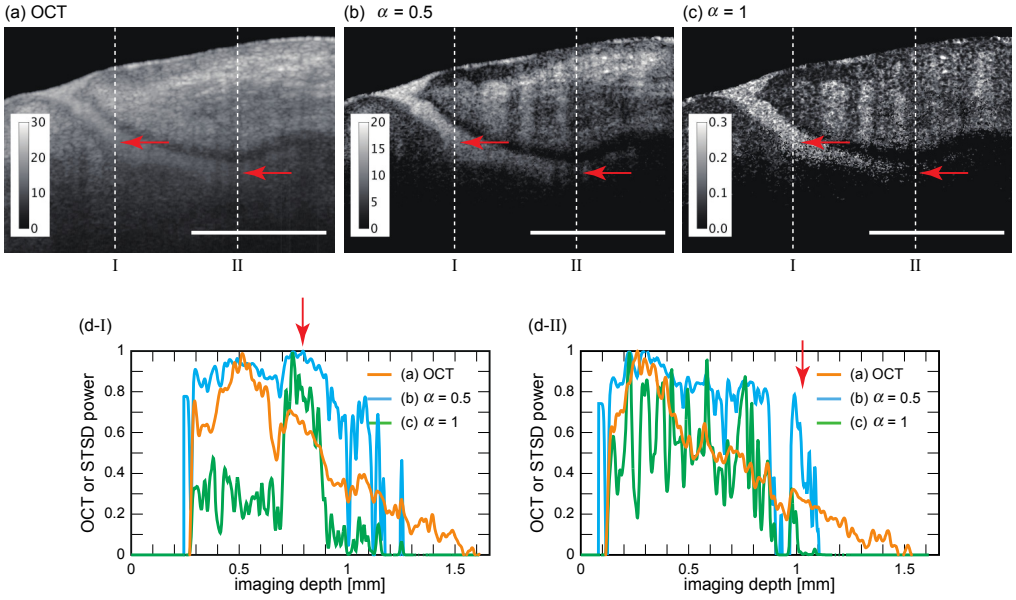

Fig. 9. (a), (b) and (c): 2D images of the LC after applying ROS, (d-I) and (d-II) are profiles of A-scans corresponding to the white dashed lines I and II in (a), (b) and (c). (a): OCT, (b): STSD (α = 0.5), (c): STSD (α = 1). Red arrows in the 2D images indicate the LC location, corresponding to the peaks pointed to with red arrows in (d). Scale bars in (a), (b) and (c) are 1 mm.

Figures 10(a)-10(c) are images of LC after applying ROS to the volunteer with the scanning area of 5.0 mm × 5.0 mm, twice the size of Figs. 9(a)-9(c). Figure 10(a) shows the OCT image, and Figs. 10(b) and 10(c) show the STSD images using α = 0.5, and 1, respectively. Figures 10(d-I) and 10(d-II) are the A-scan profiles corresponding to the white dashed lines (I) and (II) in Figs. 10(a) to 10(c), respectively. The red arrows in Figs. 10(a) to 10(c) are corresponding to the red arrows in Figs. 10(d-I) and 10(d-II), respectively. The scaling of the vertical axes in Fig. 10(d) is the same as that of Fig. 9(d). In plotting Figs. 10(d-I) and 10(d-II), the values are normalized by the peak values in 2D images (a), (b), and (c). Along the lines labeled I, the lumen images were clearly enhanced in all images (Figs. 10(a) to 10(c)), as same as in Fig. 9. The deeper end surface of the lumen image appears most clearly for α = 1 as shown if Fig. 10(d-I). However, in Fig. 10(d-II), the lumen image is faint for α = 1 and it is mostly enhanced for α = 0.5. Due to these different enhancement effects, combined use of an OCT image and STSD images make delineation of the LC lumen unambiguous. The gray scale bars in Fig. 10(a), 10(b), and 10(c) respectively indicate OCT signal power in dB, STSD (α = 0.5) signal intensity in dB, and STSD (α = 1) signal intensity in linear.

Biomedical Optics EXPRESS

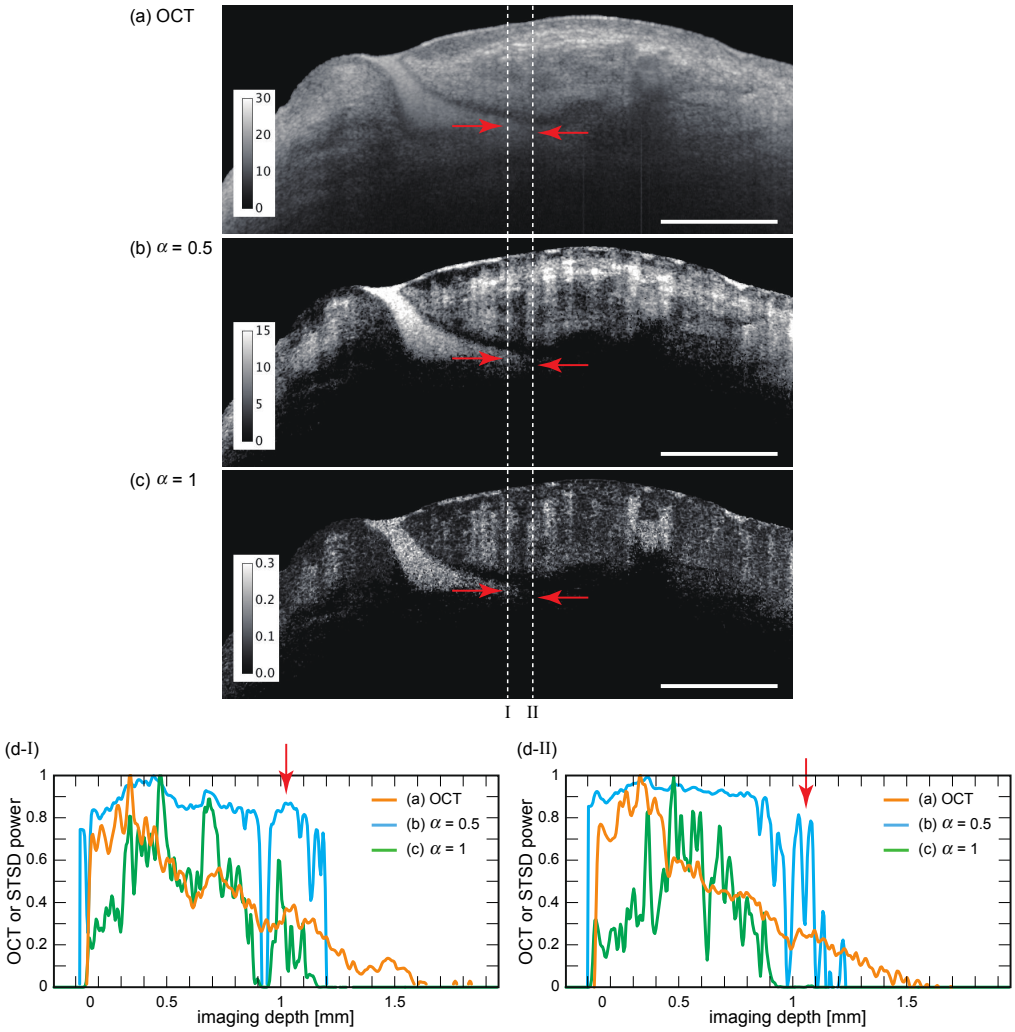

Fig. 10. (a), (b), and (c): 2D images around the LC after using ROS, (d-I), (d-II): the profiles of A-scans corresponding to the white dashed lines in (a) to (c). (a): OCT, (b): STSD (α = 0.5), (c): STSD (α = 1). Red arrows in (a) to (c) indicate the area corresponding to the red arrows in (d-I) and (d-II). Scale bars in (a), (b) and (c) are 1 mm.

3.2 Maximum intensity projection images

OCT-A images are often displayed in *en face* maximum intensity projection form (MIP). The MIP images of D-OCT-D are depicted in Fig. 11. All images were obtained from the same subject as the one imaged in Figs. 8 to 10. The scanning area of Figs. 11(a)-11(d) is 5.0 mm × 5.0 mm. To show more magnified image near the lacrimal punctum (LP), which is indicated by red arrows, we captured images with a scanning area of 2.5 mm × 2.5 mm, which are shown in Figs. 11(e)-11(h). Figures 11(a) and 11(e) are the OCT images, Figs. 11(b) and 11(f) are the STSD images with α = 0.5, Figs. 11(c) and 11(g) are the STSD images with α = 1, and Figs. 11(d) and 11(h) are the color composite images with OCT as red, STSD (α = 0.5) as green, and STSD (α = 1) as blue, respectively. These images exhibit complementary features. The image intensity of the inlet of the LP varies depending on the quantity of the remaining ROS. The OCT images of Figs. 11(a) and 11(e) show the appearance of the conjunctival surface. In the STSD (α = 0.5) images of Figs. 11(b) and 11(f), the LC intensity

Biomedical Optics EXPRESS

enhancements with ROS are not clear, while the blood-vessel networks are clear in the images. The LC intensities are greatly enhanced in the STSD (α = 1) images of Figs. 11(c) and 11(g) as highlighted with the yellow ovals. This enhancement was made by normalization with weak signal power at deep tissue. The MIP images of D-OCT-D are useful to grasp the overall shape of and lateral spreading of the LC and LP. However, they are not sufficiently sharp to segment out their outlines.

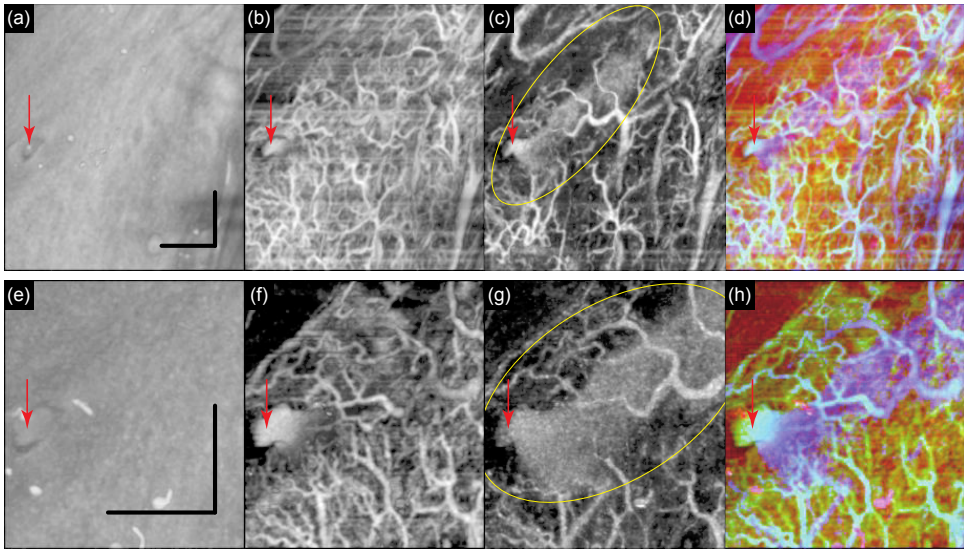

Fig. 11. *En face* maximum intensity projection (MIP) view image of the LC after applying ROS. The scanning areas of (a) to (d) are 5.0 mm × 5.0 mm and (e) to (h) are 2.5 mm × 2.5 mm, respectively. (a) and (e) are the OCT images, (b) and (f) are the STSD images with α = 0.5, (c) and (g) are the STSD images with α = 1, and (d) and (h) are the color-composite images with OCT as red, STSD α = 0.5 as green, and STSD α = 1 as blue. The red arrows in the images show the LP location in each image. Yellow ovals in (c) and (g) indicate the ROS spreading within the LC. Scale bars in (a) and (e) are 1 mm.

3.3 3D segmentation of lacrimal canaliculus

As explained above and referring to Figs. 9 and 10, the combined use of STSD images calculated using two different α values, as well as usual OCT image, made it possible to segment out LC images unambiguously. As observed in Figs. 9(d-I), 9(d-II), 10(d-I) and 10(d-II), the STSD images of the LC provide a sufficiently sharp boundary for us to delineate them from the surrounding mucosal wall in most of the region. However, the boundary of the STSD image of the LC was sometimes obscured by overlapping with the projection images of blood vessels, or the LC image was sometimes faint. These ambiguities are reduced by combining OCT and STSD images. Examples of the color image of Figs. 9(a)-9(c) are shown in Figs. 12(a)-12(c). Figure 12(a) shows the OCT image in red, Fig. 12(b) shows the STSD image for α = 0.5 in green, and Fig. 12(c) shows the STSD (α = 1) in blue, respectively. Figure 12(d) is the composited image of Figs. 12(a)-12(c). The figure shows the LP and LC are clear enough to perform segmentation. We manually segmented the LP and LC lumen for each of color-composited image, binarized it as Fig. 12(e), and then constructed 3D volume images of the LC using the Volume Viewer program of ImageJ [16].

Figures 13(a) and 13(b) are the snapshots of the 3D volume images (available online: Visualization 1 and Visualization 2) of the LC with scanning area of 5.0 mm × 5.0 mm and 2.5 mm × 2.5 mm, respectively. The white arrows in these figures show the LP location. These figures show that the inlet of the LP is funnel shaped and connected to the LC via narrow channels. LCs are not simple tubes of circular cross sections but spread to a certain extent.

Biomedical Optics EXPRESS

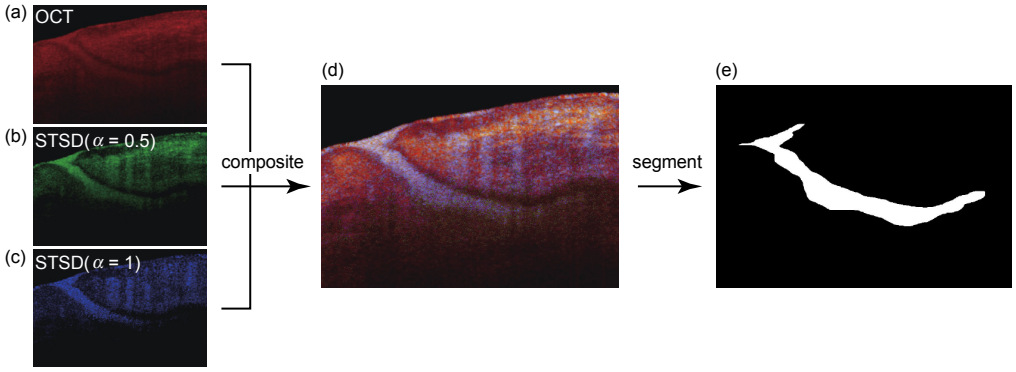

Fig. 12. An example of color-composited LC image. (a): OCT image as red, (b): STSD (α = 0.5) image as green, (c): STSD (α = 1) image as blue, (d): color-composited image of (a), (b), and (c), (d): segmented and binarized LC image.

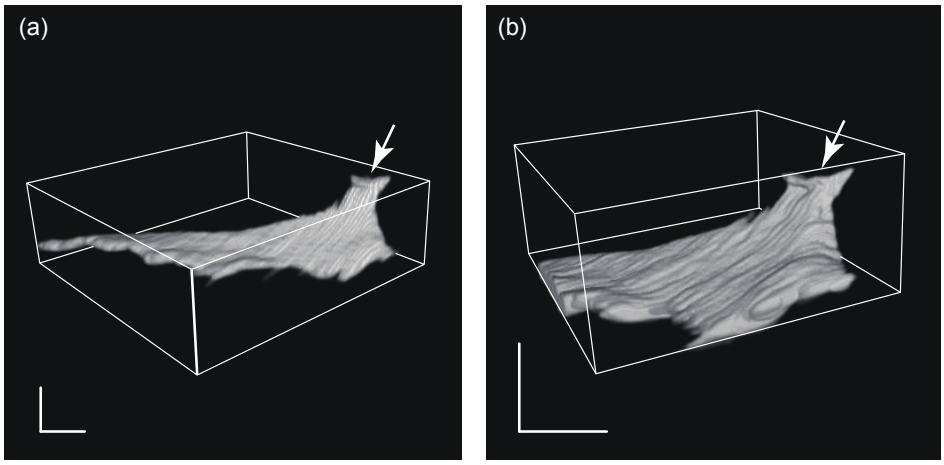

Fig. 13. The snapshots of 3D volume images of the LC under the conjunctiva (Visualization 1 and Visualization 2). The scanning area of (a) is 5.0 mm × 5.0 mm and that of (b) is 2.5 mm × 2.5 mm, respectively. The white arrows indicate the LP location. Scale bars are 1 mm.

We need to be careful about the interpretation of the obtained volume images. As shown in Fig. 1, the eyelid was flipped by the volunteer to conduct trans-conjunctiva imaging, which evidently deforms the LC shape from that of the natural position. We expected thorough and homogenous spread of extrinsic ROS within the lumen of LC, which is probable but cannot be confirmed. Therefore, 3D images of the LC lumen obtained in this study should be viewed with care and certain uncertainties taken into account.

4. Discussions and conclusion

D-OCT-D imaging of an LC and LP was conducted using the extrinsic contrast agent ROS. Image enhancement of D-OCT-D was sufficient to conduct segmentation of the LC and LP lumen. For unambiguous delineation of the lumen, composite color images were used effectively.

The present observation was only done on the lower LC and LP because of easy flipping of the eyelid. However, imaging of the upper LC and LP is also necessary for thorough diagnosis of patients. Also, imaging is limited for the LC and LP. For clinical application, deeper lacrimal passages, such as the lacrimal sac, should be attempted for future work. A promising method is the mechanical optical clearance proposed by C. Drew et al. [17]. The authors demonstrated up to threefold increased light penetration depth by mechanical

Biomedical Optics EXPRESS

indentation of skin. The shapes of the 3D images obtained in this work should be interpreted with care because they were deformed due to the flipping of the eyelid and also homogenous and complete spread of ROS within the lumen was not confirmed. To eliminate deformation by eyelid flipping, trans-skin imaging should be explored for future work. Flow dynamics of tear within the LC was not explored in this work. Imaging at different time intervals may provide information on the spreading speed of ROS within the lumen and the flow velocity of tears in the LC may be estimated.

Although preliminary, the present study demonstrated the effectiveness of D-OCT-D imaging to segment out and render 3D volumetric shapes of the LC and LP, which will be useful for clinical diagnostics.

Acknowledgments

The authors would like to thank Dr. Hisashi Yamada (Systems Engineering Inc.) for his technical advice on this experiment.

Disclosures

The authors declare that there are no conflicts of interest related to this article.

References

1. J. K. Kanski, "Lacrimal Drainage System," *Clinical Ophthalmology: A Systematic Approach* (Butterworth Heinemann) (2007), pp. 151–164.
2. M. Fujimoto, A. Uji, K. Ogino, T. Akagi, and N. Yoshimura, "Lacrimal canaliculus imaging using optical coherence tomography dacryography," Sci. Rep. **8**(1), 9808 (2018).
3. M. J. Ali, "Lacrimal Pathologies and Optical Coherence Tomography," *Atlas of Lacrimal Drainage Disorders* (Springer, 2018), pp. 187–195.
4. "American National Standard for the Safe Use of Lasers, ANSI Z136.1-2000," Laser Institute of America, Orlando, Florida, (2000).
5. C. L. Chen and R. K. Wang, "Optical coherence tomography based angiography [Invited]," Biomed. Opt. Express **8**(2), 1056–1082 (2017).
6. J. Barton and S. Stromski, "Flow measurement without phase information in optical coherence tomography images," Opt. Express **13**(14), 5234–5239 (2005).
7. A. Mariampillai, B. A. Standish, E. H. Moriyama, M. Khurana, N. R. Munce, M. K. K. Leung, J. Jiang, A. Cable, B. C. Wilson, I. A. Vitkin, and V. X. D. Yang, "Speckle variance detection of microvasculature using swept-source optical coherence tomography," Opt. Lett. **33**(13), 1530–1532 (2008).
8. A. Mariampillai, M. K. Leung, M. Jarvi, B. A. Standish, K. Lee, B. C. Wilson, A. Vitkin, and V. X. D. Yang, "Optimized speckle variance OCT imaging of microvasculature," Opt. Lett. **35**(8), 1257–1259 (2010).
9. E. Jonathan, J. Enfield, and M. J. Leahy, "Correlation mapping method for generating microcirculation morphology from optical coherence tomography (OCT) intensity images," J. Biophotonics **4**(9), 583–587 (2011).
10. J. Enfield, E. Jonathan, and M. Leahy, "In vivo imaging of the microcirculation of the volar forearm using correlation mapping optical coherence tomography (cmOCT)," Biomed. Opt. Express **2**(5), 1184–1193 (2011).
11. Y. Jia, O. Tan, J. Tokayer, B. Potsaid, Y. Wang, J. J. Liu, M. F. Kraus, H. Subhash, J. G. Fujimoto, J. Hornegger, and D. Huang, "Split-spectrum amplitude-decorrelation angiography with optical coherence tomography," Opt. Express **20**(4), 4710–4725 (2012).
12. C. W. Merkle and V. J. Srinivasan, "Laminar microvascular transit time distribution in the mouse somatosensory cortex revealed by Dynamic Contrast Optical Coherence Tomography," Neuroimage **125**, 350–362 (2016).
13. C. W. Merkle, C. Leahy, and V. J. Srinivasan, "Dynamic contrast optical coherence tomography images transit time and quantifies microvascular plasma volume and flow in the retina and choriocapillaris," Biomed. Opt. Express **7**(10), 4289–4312 (2016).
14. J. Fingler, D. Schwartz, C. Yang, and S. E. Fraser, "Mobility and transverse flow visualization using phase variance contrast with spectral domain optical coherence tomography," Opt. Express **15**(20), 12636–12653 (2007).
15. L. An, J. Qin, and R. K. Wang, "Ultrahigh sensitive optical microangiography for in vivo imaging of microcirculations within human skin tissue beds," Opt. Express **18**(8), 8220–8228 (2010).
16. ImageJ, https://imagej.nih.gov/ij/index.html
17. C. Drew, T. E. Milner, and C. G. Rylander, "Mechanical tissue optical clearing devices: evaluation of enhanced light penetration in skin using optical coherence tomography," J. Biomed. Opt. **14**(6), 064019 (2009).